Journal of Materials Chemistry A

Accepted Manuscript

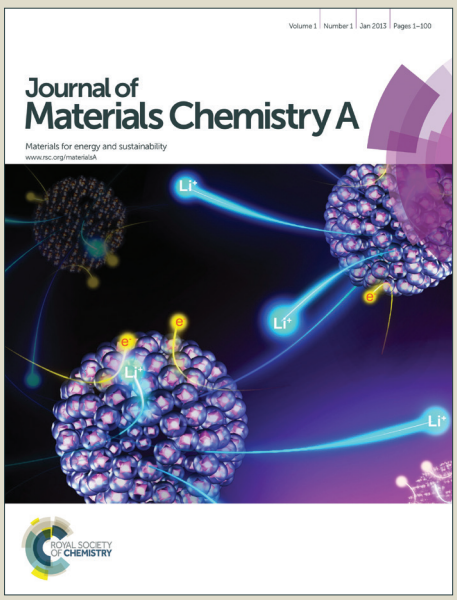

ROYAL SOCIETY OF CHEMISTRY

www.rsc.org/materialsA

Nanomeshes of Highly Crystalline Nitrogen-Doped Carbon Encapsulated Fe/Fe_3C Electrodes as Ultrafast and Stable Anodes for Li-ion Batteries

Jinqiu Zhou, Tao Qian,* Tingzhou Yang, Mengfan Wang, Jun Guo, Chenglin Yan*

College of Physics, Optoelectronics and Energy & Collaborative Innovation Center of Suzhou Nano Science and Technology, Soochow University, No.1 Shizi Street, Suzhou 215006, China. *Address correspondence to c.yan@suda.edu.cn (C. Yan) and tqian@suda.edu.cn (T. Qian).

Abstract

Fe/Fe_3C homogeneously dispersed in 2D porous Nitrogen-doped graphitic carbon nanomeshes (N-Fe/Fe_3C@C nanomeshes) was prepared by a novel template-free method using polypyrrole-Fe (PPy-Fe) coordination complex as precursor. The designed architecture is beneficial to electron transport and accommodation of the strains of Li insertion/extraction. As an anode material for Li-ion batteries, as-prepared composite exhibits a reversible capacity of 1316 mAh/g (normalized to the mass of Fe/Fe_3C in the composite) with extremely excellent cycling performance at high rate (nearly 100% capacity retention after 500 cycles) and good rate capability. The synthesis approach presents a promising route for a large-scale production of N-Fe/Fe_3C@C nanomeshes composites as extremely durable high-rate anode material for Li-ion batteries.

Introduction

Carbon nanomeshes [1-4] emerged as a new type of nanostructres have attracted great interest because of their promising applications in a wide range of areas, [5-7] in view of their fantastic architecture and tunable properties. In the field of lithium ion batteries, amorphous carbon coating was usually utilized to prevent the electrode materials from collapse, however, amorphous structure possess the drawback of low electric conductivity as compared to the crystalline counterparts, resulting in the deterioration of capacity retention and low rate capability. In contrast, highly crystalline carbon nanomesh exhibits high electric conductivity that is beneficial in enhancing rate capability and strain recommendation for lithium ion batteries (LIBs). A common synthetic strategy for the fabrication of nanomesh structure employs sacrificial templates. For example, thermally stable NaCl particles was used as template to synthesize the graphite nanomesh by He *et al*; [7] Porosity control over nitrogen-doped carbon nanosheets with uniform and tunable mesopores were achieved by employing an appropriate graphene/silica nanosheet template by Wei *et al*; [6] well-ordered thin-film nanopore arrays were formed using a block-copolymer template by Jung *et al*. [8] However, template methods are usually time consuming and costly because of the need for the synthesis of the templates and the multi-step templating process. Therefore, it is highly desirable to develop facile, scalable template-free approaches for the rational synthesis of nanomesh structures. [9]

On the basis of the available lithium storage mechanisms, Fe nanoparticles are inert to react with Li^+ and contribute nothing to electrochemical Li storage and Fe_3C can store only 1/6 Li per unit (~26 mAh g^{-1}). This does not mean that Fe/Fe_3C nanoparticles contribute nothing to the lithium storage. Actually, Fe/Fe_3C nanoparticles might serve as electrocatalysts for the reversible conversion of some components of solid electrolyte interface films, and bring extra capacity to the active materials. [10-12] As a result, Fe_3C nanomaterials as anodes for LIBs could show desirable properties based on conversion mechanics with the advantages of high capacity, non-toxicity, high abundance, high corrosion resistance, and low processing cost. However, as far as we know, Fe_3C-based nanomaterials are generally used as high-performance magnets and catalysts, [13-16] and carbides have scarcely been touched as LIB anode materials due to two troublesome obstacles. [17-18] One is the volume expansion/contraction during repeated cycling processes. Another is that the low conductivity of pristine carbides [19] also induces performance

degradation, particularly when charging and discharging at high current rates. In order to circumvent the above intractable problems, strategies have been proposed to enhance the structural stability of electrode materials. [6] It has been widely demonstrated that this problem can be partly solved in nanostructured electrode materials with various morphologies, including nanoparticles, nanosheets, nanowires, nanorods, nanotubes, and other hollow nanostructures. [20-23] Another approach is to integrate carbonaceous matrix into the active materials to form hybrid nanostructures. Typically, the carbon components in the hybrid materials are anticipated to serve dual functions: as conducting additives to promote the electron transport in the poorly conductive materials and as elastic buffer supports to enhance the stability of the electrode. [6, 24-31]

For upcoming large-scale applications, the notion of materials sustainability produced by materials made through eco-efficient processes such as renewable organic methods is crucial. Great attention has been attached to make research on fabricating electrode materials through organic methods. [32-36] Polypyrrole (PPy), as a kind of source for nitrogen doping, [37-39] is an intrinsically organic polymer material with high conductivity, storage ability, redox and capacitive current and good thermal and environmental stability. [40-44] Additionally, certain nitrogen doping is an appropriate method for strengthening the surface wettability of materials, capacity, and electric conductivity while maintaining superb cycle ability. [45] Herein, a facile, ingenious and template-free synthesis strategy was attempted to produce N-doped carbon nanomeshes encapsulated Fe/Fe_3C (N-Fe/Fe_3C@C). The fabricating process involves the novel synthesis of PPy-Fe coordination complex and the carbonization of prepared precursor. It is found that the constructed unique 2D architecture not only avoids the direct exposure of encapsulated Fe/Fe_3C to the electrolyte to preserve the structural and interfacial stabilization of Fe/Fe_3C, but also accommodate the mechanical stress induced by the volume change of the embedded Fe/Fe_3C nanoparticles as well as inhibit the aggregation of Fe/Fe_3C, which thus maintains the structural and electrical integrity. As a result, the prepared anode exhibits very high reversible specific capacity, ultrafast rate performance and especially high cycling stability. Notably, the starting materials and the synthetic processes are both viable for large-scale production, making this approach particularly attractive for practical applications.

Experimental

Materials preparation: PPy spheres were synthesized according to the reported method. [46] 0.35 g of $FeCl_2$ and 20.0 mL of H_2O_2 were added to the deep dark solution of PPy spheres. After continuously stirring overnight, the deep dark solution became bright yellow and transparent. The solution was dried at vacuum to obtain a dark yellow product. After that, as-prepared materials were heated at 900 ℃ for 2 h in a tube furnace under flowing Ar (200 sccm) and H_2 (40 sccm) atmosphere to obtain N-Fe/Fe_3C@C nanomeshes. To obtain N-doped carbon nanomeshes, the N-Fe/Fe_3C@C was leached in 6 M HNO_3 solutions for 24 h and then washed with deionized water for three times.

Physical characterization: Elemental analysis was made on x-ray photoelectron spectrometer (Kratos Axis Ultra Dld, Japan). Fourier-transformed infrared (FT-IR) spectra were recorded on a Nicolet is 50 spectrometer (ThemoFisher Scientific, America). UV-Vis-NIR Spectrophotometer (SHIMADZU company, Japan) was used to perform UV-Vis-NIR spectra analysis. The morphology was observed with field emission scanning electron microscopy (FESEM, SU8010, Japan), and field emission transmission electron microscopy (FETEM, FEI Tecnai G2 F20 S-TWIN TMP, Hongkong). X-ray diffraction (XRD) measurements were taken on a Rigaku D/max-2000PC diffractometer with Cu KR radiation. Thermogravimetric analysis (TGA) was performed with a SDT 2960 (TA Instruments) up to 800 °C at a heating rate of 10 °C/min in air. Raman spectra were recorded on the HR800 (HORIBA Jobin Yvon) Raman spectrometer. Inductive Coupled Plasma (ICP) Emission Spectrometer (OPTIMA 8000) was used to determine the content of Fe element.

Electrochemical evaluation: Electrodes were prepared by mixing the as-prepared powder (70 wt. %), carbon black (20 wt. %) and polytetrafluoroethylene binder (PTFE, 10 wt. %), casted onto a piece of nickel foam with a mass loading of ~0.8 mg cm^{-2}. Electrode sheets were dried under vacuum at 60 ℃ for 24 h. Coin cells (CR2025) were fabricated with fresh lithium foil as the counter electrode, 1 mol L^{-1} $LiPF_6$ dissolved in a mixture of ethylene carbonate (EC), ethyl methyl carbonate (EMC) and diethyl carbonate (DEC) (4:3:3 vol. %) as the electrolyte, and Celgard 2400 as the separator. The assembly of the cell was conducted in an Ar-filled glove box followed by an overnight aging treatment before the test. Cyclic voltammetry (CV) measurement was conducted at 0.1 mV/s within the range of 0.0-3.0 V on CHI 660E electrochemical workstation. Electrochemical impedance spectroscopy (EIS) was also performed on this

electrochemical workstation over the frequency range from 100 kHz to 0.01 Hz. The cycle life and rate capability of the cells were tested within a voltage window of 0.0-3.0 V (*vs.* Li^+/Li) by using a battery testing system (LAND CT 2001A, Wuhan, China) at room temperature.

Results and discussions

The fabrication process for the N-Fe/Fe_3C@C hybrid nanomeshes principally consists of two steps as shown in Fig. 1. The first step involves the synthesis of PPy-Fe coordination complex. After the addition of extra $FeCl_2$ and H_2O_2, the color of the solution transformed from deep dark to bright yellow and finally to transparent (Fig. 2A). In the second step, PPy-Fe complex was calcined at 900 ℃ for 2 h under flowing Ar and H_2 atmosphere, thus yielding discrete and homogeneous N-carbon-encapsulated Fe/Fe_3C uniformly dispersed in graphitic carbon nanomeshes. To explore the formation mechanism of PPy-Fe coordination complex, the structural changes in the PPy-Fe coordination complex were investigated by comparing the XPS spectra (Fig. 2B). In the survey region from 0 to 800 eV, it is evident that C, O, and N elements all exist in two samples while Fe element appears in the PPy-Fe only. The high-resolution C1s (Fig. S1A) is clearly divided into four components at 284.7, 285.3, 286.5 and 288.3 eV corresponding to C-C, C-N, C=N and C=O. [46] The intensity of C=N is weakened, while the intensity of C-N is enhanced after coordinating, which implies the coordination reaction of Fe ions and N atoms. Comparing N1s XPS spectrum (Fig. S1B), the appearance of $–NH^+–$ (401.5 eV) [46] peak indicates that the N atoms coordinated with Fe ions, whereas the H ions are partly remained. Additionally, the Fe2p peak appeared at 709.8 eV further justifies the successful synthesis of PPy-Fe coordination complex (Fig. S1C). FT-IR analysis of the pure PPy and PPy-Fe coordination complex was performed to recognize the change of the interactions within the complex after the formation of the complex (Fig. 2C). The stretching positions of the C=C backbone (at 1549 cm^{-1}), the C–C ring (at 1445 cm^{-1}) and C–N (at 1380 cm^{-1}) arising from PPy, which was further confirmed by the emergence of the pyrrole ring vibration located at 964 cm^{-1}.[33] The presence of an imine-like nitrogen (C=N–, at 2200 cm^{-1}) [46] and C=O structure (at 1700 cm^{-1}) [47] is consistent with the structure of overoxidized polypyrrole. After the coordination, peaks at 1380 cm^{-1} (C-N stretching vibration) [35] and 750 cm^{-1} (C-O stretching vibration in epoxide) are enhanced and the new peak at about 3050 cm^{-1} (free hydrogen atoms) appears，indicating the occurrence of the coordination reaction. The disappearance of the peak at 2200

cm^{-1} indicates that the imine-like nitrogen ring changes to pyrrole-like N through the formation of the Fe–N bond, which was the evidence of the extrapolation from the XPS spectra.

The morphologies of N-Fe/Fe_3C@C nanomeshes were examined by SEM and TEM, which are shown in Figure 3. The low-magnification image in Fig. 3A shows a thin wrinkled "paperlike" structure with a thickness of about 150 nm. Fig. 3B presents typical low-magnification TEM images of Fe/Fe_3C@C nanosheets, which demonstrates that these micrometer-sized nanosheets appear as a foam-like porous graphitic structure hybridized with Fe/Fe_3C particles, as shown in Fig. 3C. High-magnification TEM images (Fig. 3D) of N-Fe/Fe_3C@C nanomeshes clearly reveal that the carbon meshes present a very high degree of graphitization showing lattice fringe with d-spacings of 0.34 nm which are in good agreement with that of the (002) planes of graphite. [6, 48] A well-defined crystalline lattice spacing of 0.21 nm was observed in Fig. 3D, which is consistent with the (211) diffraction peak of Fe_3C [12] and the (110) plane of metallic Fe. [49] As shown in Fig. 4A, the diffraction peak at 26.5 ° corresponds to the (002) plane of graphitic carbon, while the peaks located at 44.8 ° and 65.1 ° are attributed to the in-situ formation of of Fe (JCPDS, No. 89-7194). The rest of diffraction peaks are characteristics of the crystalline planes of Fe_3C species (JCPDS, No. 89-2867). [10-13] To support the existence of Fe_3C, the selected area electron diffraction (SAED) pattern [50-52] of N-Fe/Fe_3C@C nanomeshes is shown in the insert of Fig. 4A. The diffraction peaks marked by white arrows are the characteristic peaks (200), (040) and (141) of Fe_3C with lattice spacings differing from Fe, which provides powerful evidence supporting the existence of Fe_3C. Additionally, the broad peak around $2\theta=22$ ° is associated with the planar aromatic rings of pyrrole, [53-55] further confirming the nitrogen-doped structure. XPS spectrum was carried out in the region of 0–1100 eV, as shown in Fig. 4B. The distinct peaks at 285 and 532 eV correspond to C1s and O1s, however, no Fe2p signal was observed. [6, 56] The high-resolution C1s (Fig. S4A) is clearly divided into four components at 284.7, 285.3, 286.6 and 288.7 eV corresponding to C-C, C-N, and C=N, C=O, respectively. Comparing with the C1s spectrum of the PPy-Fe coordination complex, it is evident that the intensity of C=O is weakened and the intensity of C-C is enhanced after carbonization. As shown in Fig. S4B, a trivial N1s signal was observed with a share of nitrogen atoms (~3.53 wt. %, Fig. 4C). The Raman spectrum was shown in Fig. 4D wherein G band occurs at 1596 cm^{-1}(G means "graphitic") and D band occurs at 1340 cm^{-1} (D means "disorder"). [57] The value of I_D/I_G reflecting the degree of

crystallinity of carbon structures [6] is determined to be ~1. It is well accepted that the D band may be activated or enhanced by in-plane substitutional heteroatoms or introduction of defects. N doping is very effective in introducing defects into the structure, which is consistent with a large body of literature. TGA (seen in Fig. S4D), carried out in air at a heating rate of 10 ^{o}C/min from room temperature to 800^{o} C was used to determine the mass of Fe/Fe_3C in the composite. According to the remaining weight of Fe_2O_3 (45.6 wt. %) due to the oxidation reaction of Fe/Fe_3C, the original fraction of Fe/Fe_3C is calculated to be ~34.2 wt. %. Additionally, ICP Emission Spectrometer was used to further determine the Fe content of N-Fe/Fe_3C@C nonomeshes. The result (~34 wt. %) is according with that of TGA.

CV provides more details for the electrode redox processes during the electrochemical reaction. Fig. 5A shows the first four CV curves of the N-Fe/Fe_3C@C nonomesh electrodes between 0.0 and 3.0 V at a scan rate of 0.1 m V/s. It is clear that the CV curve of the first cycle is somewhat different from those of the subsequent cycles. A well-defined peak is observed ~ 0.5 V (*vs.* Li^+/Li) while the big slope corresponds to Li^+ insertion into carbon. However, the peak intensity drops from the second cycle, arising from irreversible side reactions on the electrode surfaces and interfaces mainly due to solid electrolyte interface (SEI) formation. The electrode exhibits obvious redox peaks and different potential ranges for lithium storage. The distinct peaks appear at 0.7 V and 1.4 V due to the polarization along with cycling during discharge and at 1.6 and 2.0 V during charge in the subsequent cycling. It is noteworthy that, after the first cycle, the voltage current curves almost overlapped, which is consistent with the outstanding cycling stability of the material, indicating that a stable SEI film formed in the first cycle can safeguard the structural integrity of N-Fe/Fe_3C@C nanomesh composite during subsequent charge-discharge cycles, thus leading to stable and superior reversibility of the sample. [6, 15, 33] Fe/Fe_3C nanoparticles play an indispensable role here and work within a novel mechanism, which can be evidently justified by that the CV profile of N-Fe/Fe_3C@C is different from that of N-doped carbon nanomeshes electrodes (Fig. S5). Besides the similar peak in the first cycle for the SEI formation, no obvious reduction and oxidation peaks were observed in Fig. S5 and the area in the subsequent cycles was much lower than that of N-Fe/Fe_3C@C electrode.[15] Fig. 5B shows representative discharge/charge voltage profiles at a current density of 300 mA g^{-1} between 0.0 and 3.0 V, which delivers a very high lithium storage capacity of 3539 mAh g^{-1} during the initial discharge process, and the Coulombic Efficiency in the initial cycle is 50% and

increases to nearly100% during the subsequent cycles. It should be emphasized that no obvious change in both charge and discharge profiles is observed even after 100 cycles, indicating the extraordinarily stable performance of the nanomesh electrodes. To highlight the superiority of the unique N-Fe/Fe_3C@C nanomeshes for lithium storage material, we tested the cycle performance of the electrode at a current density of 300 mA g^{-1} between 0.0 and 3.0 V *vs.* Li^+/Li (Fig. 5C). Apparently, the reversible capacity reaches 1316 mAh g^{-1} and demonstrates excellent cyclic retention. EIS was conducted at frequencies from 100 kHz to 0.01 Hz. Fig. 5D shows the EIS profiles of the as-prepared coin cell at different status: before cycling and after 1^{st}, 5^{th}, 15^{th} and 50^{th} charging process. The R_{CT} (charge transfer resistance, approximate to the diameter of the semicircle) obviously reduces after 1^{st}, 5^{th}, 15^{th} cycle due to the building of Li-ion transport channels and then increases in the following cycles due to the polarization of the electrode. [58]

In addition to their superior stable performance, the N-Fe/Fe_3C@C nanomesh electrode also shows outstanding rate performance (Fig. 5E). To improve the rate capability of electrodes for LIBs, in our work, highly crystalline carbon nanomesh rather than amorphous carbon structures was utilized for fast electron transport. As shown in Figure 5E, the capacity only decreases from 1312, 1021, 836, 747, 696, 626, 564, 492, 474, 418, 334, t 279, 205, 175 to 117 mAh g^{-1} when the current density increases from 0.3C, 0.9C, 1.8C, 2.7C, 3.6C, 5.4C, 7.2C, 10.8C, 14.4C, 18C, 27C, 36C, 54C, 72C, 144C (1C=1 A g^{-1}). Surprisingly, even at an ultrahigh charge/discharge rate of 144 C, it can still deliver a reversible capacity of 120 mAh g^{-1}. Moreover, when the current rate is finally returned to its initial current density of 0.9C and 0.3C after a total of 80 cycles, a capacity of 1114 and 1455 mAh g^{-1} respectively is still recoverable without any losses. The durability of this anode working at higher rate (Fig. 5F) was investigated under the current density of 3600 mA g^{-1} for 500 cycles with reversible capacity of 819 mAh g^{-1}, further demonstrating extraordinary superior cycling stability of this structure even at ultrahigh charge/discharge rates.

Conclusions

In summary, to achieve ultrafast and stable anodes for lithium ion batteries, a new type of nitrogen doped Fe/Fe_3C@C nanomeshes composites was fabricated by means of a template-free organic coordination complex method. The prepared electrodes deliver a high capacity of ~1316 mAh g^{-1} and ultrafast charge/discharge rate of 144 C, as well as nearly 100% capacity retention

after 500 cycles. Our reported novel and high-yield strategy through organic coordination complex route as in situ doping resources can be extended to build a variety of other interesting materials for stable and ultrafast LIBs.

Acknowledgements: We acknowledge the support from the "Thousand Talents Program", the Natural Science Foundation of Jiangsu Province of China (no.BK20140315), the National Natural Science Foundation of China (no. 51402202), the National Basic Research Program of China (no. 2015CB358600), Jiangsu Shuangchuang Plan, and the Priority Academic Program Development of Jiangsu Higher Education Institutions (PAPD).

Notes and references

1 J. W. Bai, X. Zhong, S. Jiang, Y. Huang and X. F. Duan, *Nature Nanotech.*, 2010, **5,** 190.

2 S. Berner, M. Corso, R. Widmer, O. Groening, R. Laskowski, P. Blaha, K. Schwarz, A. Goriachko, H. Over, S. Gsell, M. Schreck, H. Sachdev, T. Greber and J. Osterwalder, *Angew. Chem. Int. Ed.*, 2007, **46,** 5115.

3 H. S. Ahin and S. Ciraci, *Phys. Rev. B*, 2011, **84,** 035452.

4 U. Schlickum, R. Decker, F. Klappenberger, G. Zoppellaro, S. Klyatskaya, M. Ruben, I. Silanes, A. Arnau, K. Kern, H. Brune and J. V. Barth, *Nano Lett.*, 2007, **7,** 3813.

5 H. P. Zhao, C. L. Wang, R. Vellacheri, M, Zhou, Y. Xu, Q. Fu, M. H. Wu, F. Grote and Y. Lei, *Adv. Mater.*, 2014, **26,** 7654.

6 W. Wei, H. W. Liang, K. Parvez, X. D. Zhuang, X. L. Feng and K. Mullen, *Angew. Chem. Int. Ed.*, 2014, **53,** 1570.

7 C. N. He, S. Wu, N. Q. Zhao, C. S. Shi, E. Z. Liu and J. J. Li, *ACS Nano*, 2013, **7,** 4459.

8 Y. S. Jung and C. A. Ross, *Small*, 2009, **5,** 1654.

9 A. Q. Pan, H. B. Wu, L. Yu and X. W. Lou, *Angew. Chem. Int. Ed.*, 2013, **125,** 2282.

10 L. W. Su, Y, R, Zhong and Z. Zhou, *J. Mater. Chem. A*, 2013, **1,** 15158.

11 L. W. Su, Z. Zhou and P. W. Shen, *J. Phys. Chem. C*, 2012, **116,** 23974.

12 L. W. Su, Z. Zhou, X. Qin, Q. W. Tang, D. H. Wu and P. W. Shen, *Nano Energy*, 2013, **2,** 276.

13 Y. Hou, T. Z. Huang, Z. H. Wen, S. Mao, S. M. Cui and J. H. Chen, *Adv. Energy Mater.*, 2014, **4,** 1400337.

14 J. S. Lee, G. S. Park, S. T. Kim, M. L. Liu and J. Cho, *Angew. Chem. Int. Ed.*, 2013, **125,** 1060.

15 Z. H. Wen, S. Q. Ci, F. Zhang, X. L. Feng, S. M. Cui, S. Mao, S. L. Luo, Z. He and J. H. Chen, *Adv. Mater.*, 2012, **24,** 1399.

16 Y. Hu, J. O. Jensen, W. Zhang, L. N. Cleemann, W. Xing, N. J. Bjerrum and Q. F. Li, *Angew. Chem. Int. Ed.*, 2014, **53,** 3675.

17 M. Naguib, J. Come, B. Dyatkin, V. Presser, P. L. Taberna, P. Simon, M. W. Barsoum and Y. Gogotsi, *Electrochem. Commun.*, 2012, **16,** 61.

18 L. W. Su, Z. Zhou and P. W. Shen, *Electrochim. Acta*, 2013, **87,** 180.

19 K. Ichikawa and M. Achikita, *Mater. Trans.*, 1993, **16,** 718.
20 Y. G. Guo, J. S.Hu, L. J. Wan, Adv. Mater. 2008, **20,** 2878.
21 N. Kang, J. H. Park, J. Choi, J. Jin, J. Chun, I. G. Jung, J. Jeong, J. G. Park, S. M. Lee and H. J. Kim, *Angew. Chem. Int. Ed.*, 2012, **51,** 6626.
22 Z. Y. Wang, L. Zhou and X. W. Lou, *Adv. Mater.*, 2012, **24,** 1903.
23 Z. M. Cui, L. Y. Jiang, W. G. Song and Y. G. Guo, *Chem. Mater.*, 2009, **21,** 1162.
24 S. B. Yang, X. L. Feng, S. Ivanovici and K. Mullen, *Angew. Chem. Int. Ed.*, 2010, **49,** 8408.
25 X. J. Zhu, Y. W. Zhu, S. Murali, M. D. Stoller and R. S. Ruoff, *ACS Nano,* 2011, **5,** 3333.
26 Z. C. Yang, J. G. Shen and L. A. Archer, *J. Mater. Chem.*, 2011, **21,** 11092.
27 T. Yoon, C. Chae, Y. K. Sun, X. Zhao, H. H. Kung and J. K. Lee, *J. Mater. Chem.*, 2011, **21,** 17325.
28 E. Kang, Y. S. Jung, A. S. Cavanagh, G. H. Kim, S. M. George, A. C. Dillon, J. K. Kim and J. Lee, *Adv. Funct. Mater.*, 2011, **21,** 2430.
29 J. S. Chen, Y. M. Zhang and X. W. Lou, *ACS Appl. Mater. Interfaces,* 2011, **3,** 3276.
30 J. Liu, Y. Zhou, F. Liu, C. Liu, J. Wang, Y. Pan and D. Xue, *RSC Adv.*, 2012, **2,** 2262.
31 Q. Qu, S. Yang and X. Feng, *Adv. Mater.*, 2011, **23,** 5574.
32 S. W. Wang, L. J. Wang, K. Zhang, Z. Q. Zhu, Z. L. Tao and J. Chen, *Nano Lett.*, 2013, **13,** 4404.
33 M. Armand, S. Grugeon, H. Vezin, S. Laruelle, P. Ribière, P. Poizot and J. M. Tarascon, *Nature Mater.*, 2009, **8,** 120.
34 F. R. Brushett, J. T. Vaughey and A. N. Jansen, *Adv. Energy Mater.*, 2012, **2,** 1390.
35 Y. Mao, Q. Y. Kong, B. K. Guo, X. P. Fang, X. W. Guo, L. Shen, M. Armand, Z. X. Wang and L. Q. Chen, *Energy Environ. Sci.*, 2011, **4,** 3442.
36 Y. Mao, Q. Y. Kong, L. Shen, Z. X. Wang and L. Q. Chen, *J. Power Sources.*, 2014, **248,** 343.
37 F. H. Du, B. Li, W. Fu, Y. J. Xiong, K. X. Wang and J. S. Chen, *Adv. Mater.*, 2014, **26,** 6145.
38 T. Qian, C. F. Yu, S. S. Wu and J. Shen, *Biosens. Bioelectron.*, 2013, **50,** 157.
39 T. Z. Yang, T. Qian, M. F. Wang, J. Liu, J. Q. Zhou, Z. Z. Sun, M. Z. Chen and C. L. Yan, *J. Mater. Chem. A,* 2015, **3,** 6291.
40 T. Qian, N. Xu, J. Q. Zhou, T. Z. Yang, X. J. Liu, X. W. Shen, J. Q. Liang and C. L. Yan, *J. Mater. Chem. A,* 2015, **3,** 488.
41 X. J. Liu, T. Qian, N. Xu, J. Q. Zhou, J. Guo and C. L. Yan, *Carbon,* 2015, **92,** 348.

42 T. Qian, S. S. Wu and J. Shen, *Chem. Commun.*, 2013, **49,** 4610.
43 T. Qian, X. Zhou, C. F. Yu, S. S. Wu and J. Shen, *J. Mater. Chem. A,* 2013, **1,** 15230.
44 C. Zhou, Y. W. Zhang, Y. Y. Li and J. P. Liu, *Nano Lett.*, 2013, **13,** 2078.
45 L. F. Chen, X. D. Zhang, H. W. Liang, M. G. Kong, Q. F. Guan and P. Chen, *ACS Nano*, 2012, **6,** 7092.
46 D. H. Nam, S. J. Lim, M. J. Kim and H. S. Kwon, *RSC Adv.*, 2013, **3,** 16102.
47 Y. F. Li and R. Y. Qian, *Electrochim. Acta*, 2000, **45,** 1727.
48 J. Qu, Y. X. Yin, Y. Q. Wang, Y. Yan, Y. G. Guo and W. G. Song, *ACS Appl. Mater. Interfaces*, 2013, **5,** 3932.
49 M. Q. Wang, W. H. Yang, H. H. Wang, C. Chen, Z. Y. Zhou and S. G. Sun, *ACS Catal.*, 2014, **4,** 3928.
50 M. M. Lu, W. Q. Cao, H. L. Shi, X. Y. Fang, J. Yang, Z. L. Hou, H. B. Jin, W. Z. Wang, J. Yuan and M. S. Cao, *J. Mater. Chem. A,* 2014, **2,** 10540.
51 B. Wen, X. X. Wang, W. Q. Cao, H. L. Shi, M. M. Lu, G. Wang, H. B. Jin, W. Z. Wang, J. Yuan and M. S. Cao, *Nanoscale,* 2014, **6,** 5754.
52 H. J. Yang, M. S. Cao, Y. Li, H. L. Shi, Z. L. Hou, X. Y. Fang , H. B. Jin, W. Z. Wang and J. Yuan, *Adv. Optical Mater.*, 2014, **2,** 214.
53 X. F. Lu, D. M. Chao, J. Y. Chen, W. J. Zhang and Y. Wei, *Mater. Lett.*, 2006, **60,** 2851.
54 S. Y. Jing, S. X. Xing, L. X. Yu and C. Zhao, *Mater. Lett.*, 2007, **61,** 4528.
55 L. L. Qiu, S. C. Zhang, L. Zhang, M. M. Sun and W. K. Wang, *Electrochim. Acta*, 2010, **55,** 4632.
56 Y. Chen, B. H. Song, M. Li, L. Lu and J. M. Xue, *Adv. Funct. Mater.*, 2014, **24,** 319.
57 J. H. Kaufman and S. Metin, *Phys. Rev. B.*, 1989, **39,** 13053.
58 Z. P. Song, Y. M. Qian, X. Z. Liu, T. Zhang, Y. B. Zhu, H. T. Yu, M. Otanibd and H. S. Zhou, *Energy Environ. Sci.*, 2014, **7,** 4077.

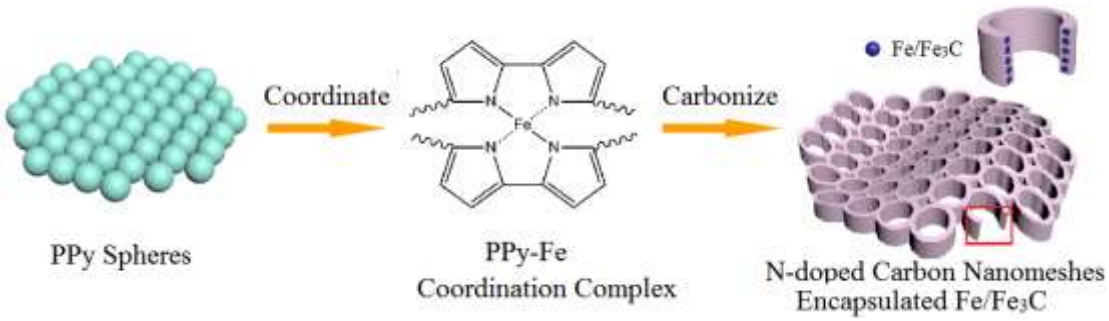

Fig. 1. Schematic representation of the synthesis of N-Fe/Fe_3C@C nanomeshes.

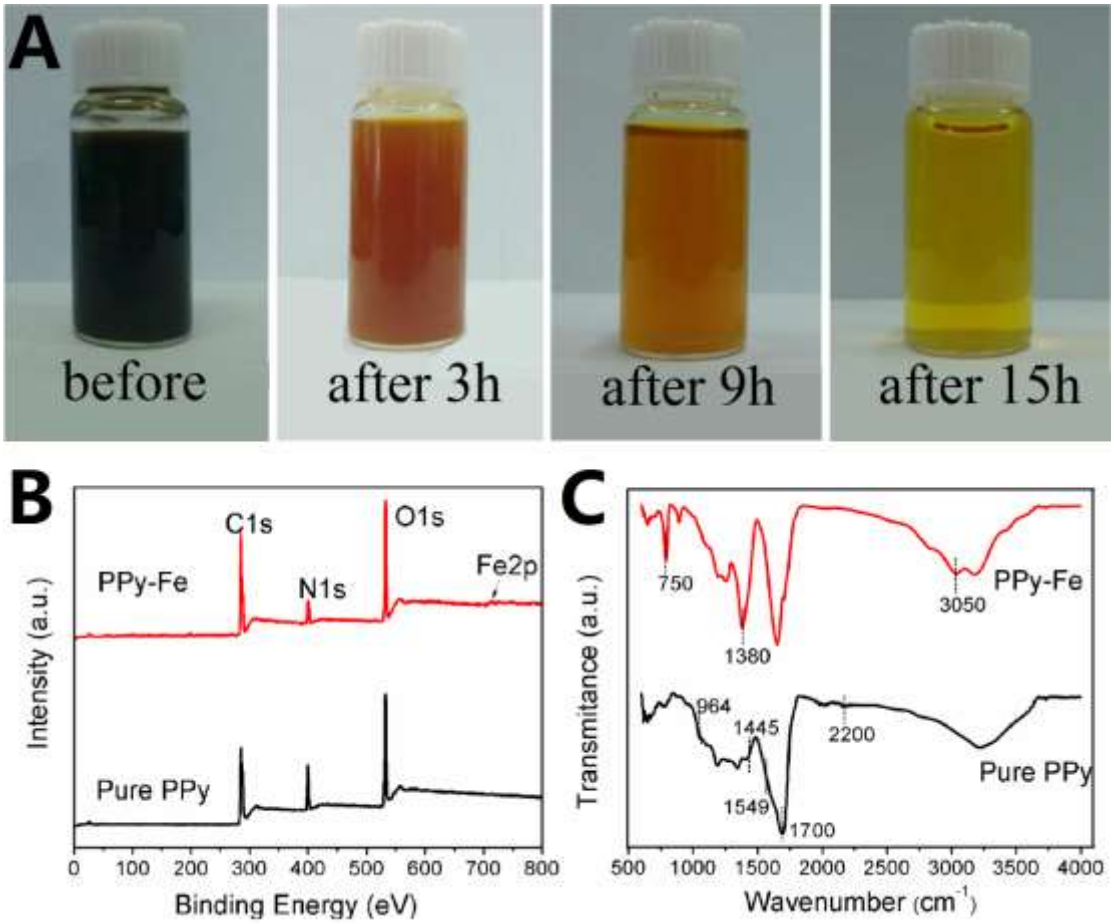

Fig. 2. (A) The color of the obtained solution (before, after 3 h, 9 h, 15h from left to right) (B) The full XPS spectra (C) FT-IR spectra of the pure PPy and PPy-Fe coordination complex.

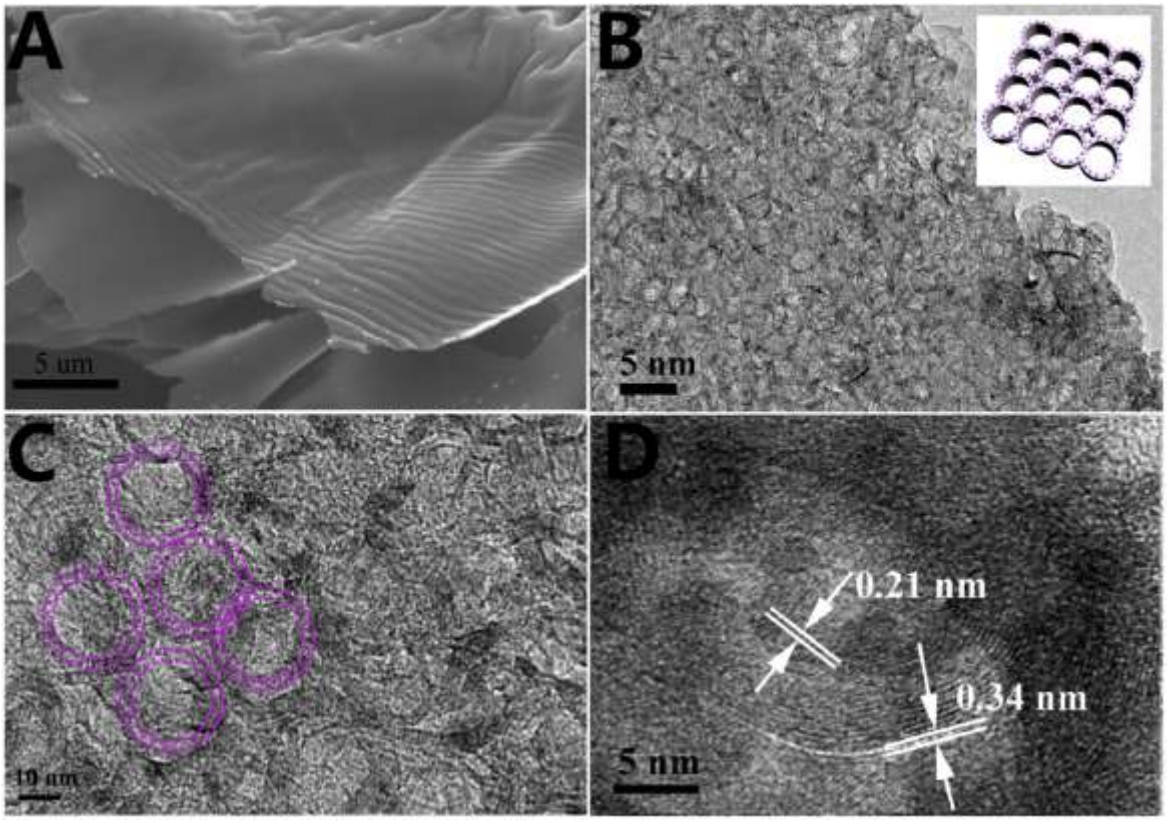

Fig. 3. (A) SEM, (B, C, D) TEM images of the nitrogen doped Fe/Fe_3C@C nanomeshes. The inset in Figure 3B is a top-view schematic for the nitrogen doped Fe/Fe_3C@C nanomeshes.

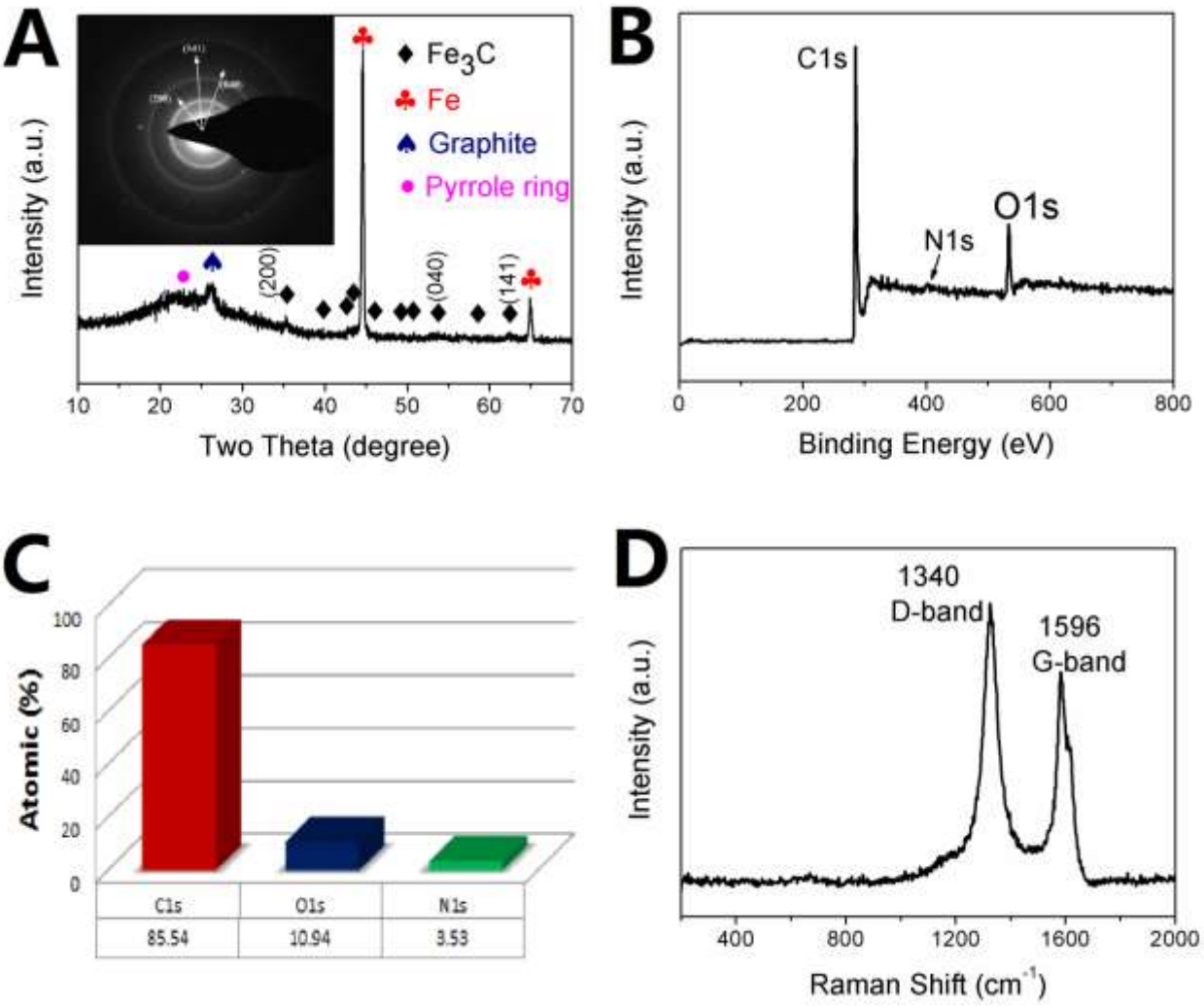

Fig. 4. (A) XRD pattern (B) Full XPS spectrum (C) The element content of the N-Fe/Fe_3C@C nanomeshes obtained from XPS measurement and (D) Raman spectrum of the N-Fe/Fe_3C@C nanomeshes. The insert of (A) is the SAED pattern of N-Fe/Fe_3C@C nanomeshes.

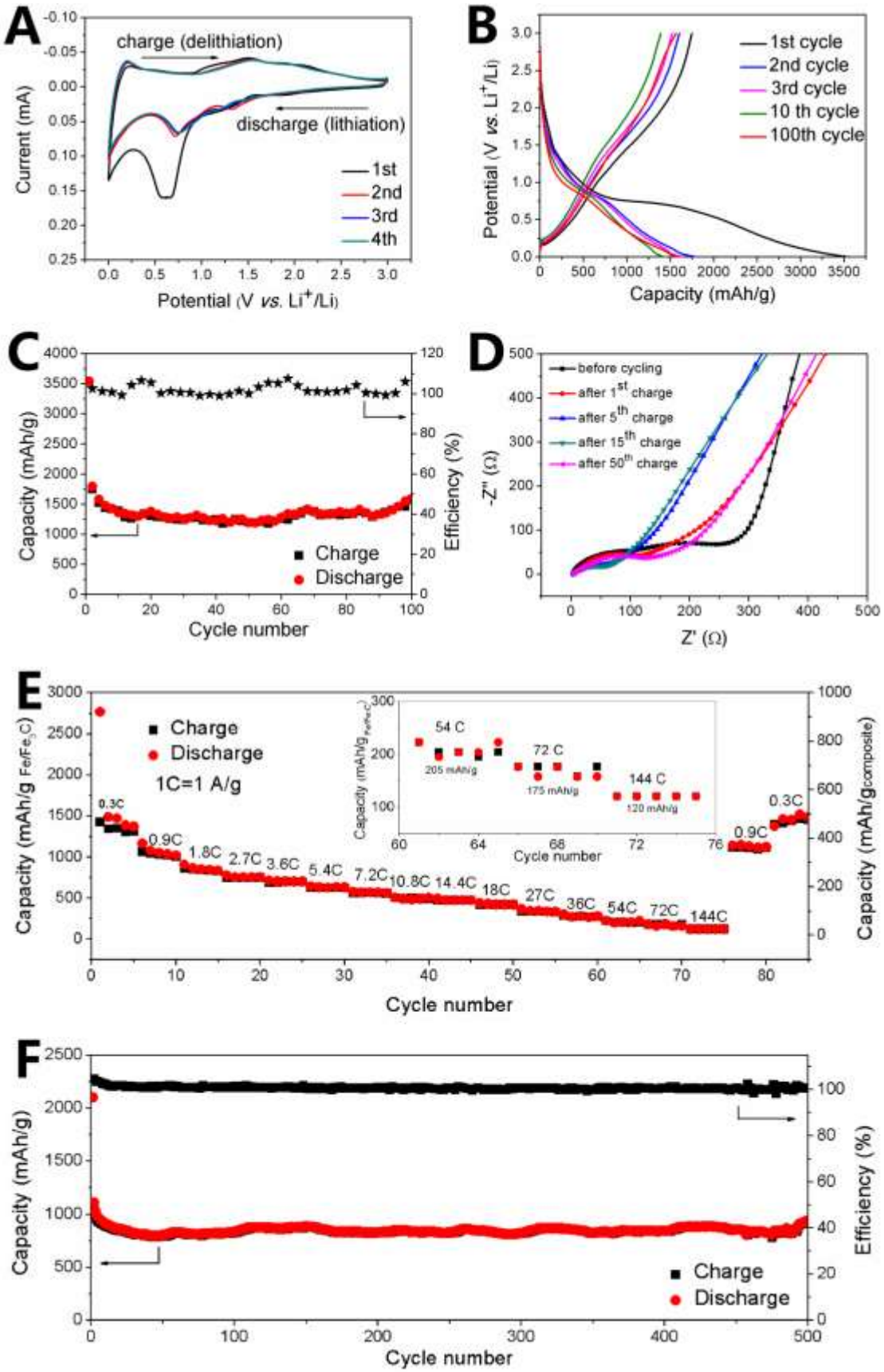

Fig. 5. (A) Representative CV curves of an electrode based on N-Fe/Fe_3C@C nanomeshes obtained at a voltage range of 0.0 to 3.0 V (*vs.* Li^+/Li) and potential scan rate of 0.1 mV/s. (B) Voltage profiles plotted for the first, second, third, 10th, 100th cycles at a current density of 300 mA g^{-1}. (C) Charge/discharge capacities and the efficiency of the prepared coin cell at a current density of 300 mA g^{-1}. (D) Nyquist plots at fresh coin cells over the frequency range from 100 kHz to 0.01 Hz. (E) Charge/discharge capacity at various rates for 90 cycles, inset shows the rate capability at higher current rates. (F) Charge/discharge capacities and the efficiency of the electrode at a high current density of 3600 mA g^{-1} for 500 cycles. All the specific capacities and current densities are calculated based on the mass of Fe/Fe_3C in the composite.

A table of contents entry

Nanomeshes of highly crystalline nitrogen-doped carbon encapsulated Fe/Fe_3C electrodes as ultrafast and stable anodes for Li-ion batteries have been demonstrated.